Bulletin of the Seismological Society of America. Vol. 66, No. 5, pp. 1485–1499. October 1976

INVERSION OF THE BODY WAVES FROM THE BORREGO MOUNTAIN EARTHQUAKE TO THE SOURCE MECHANISM

By L. J. Burdick and George R. Mellman

ABSTRACT

The generalized linear inverse technique has been adapted to the problem of determining an earthquake source model from body-wave data. The technique has been successfully applied to the Borrego Mountain earthquake of April 9, 1968. Synthetic seismograms computed from the resulting model match in close detail the first 25 sec of long-period seismograms from a wide range of azimuths. The main shock source-time function has been determined by a new simultaneous short period-long period deconvolution technique as well as by the inversion technique. The duration and shape of this time function indicate that most of the body-wave energy was radiated from a surface with effective radius of only 8 km. This is much smaller than the total surface rupture length or the length of the aftershock zone. Along with the moment determination of $M_o = 11.2 \times 10^{25}$ dyne-cm, this radius implies a high stress drop of about 96 bars. Evidence in the amplitude data indicates that the polarization angle of shear waves is very sensitive to lateral structure.

Introduction

Since the introduction of simple theoretical fault models, many investigators have attempted to infer details of earthquake faulting by comparing far-field body-wave recordings with model predictions. They have found that most deep and intermediate events have simple wave shapes which can be easily explained with smooth dislocation models, (Mikumo, 1971, a and b; Teng and Ben Menahem, 1965; Burdick and Helmberger 1974) but that shallow earthquakes have very complex wave forms. Until recently, this was interpreted to mean that shallow events have fundamentally more complex fault surfaces and time histories. By determining the response of a layered half-space to a shallow double-couple point source, Helmberger (1974), Fukao (1971), and Hudson (1969), among others, have shown that this interpretation is not entirely correct because much of the wave-form complexity is caused by the interaction of the source with the free surface. Thus, it will once again be worthwhile to address the question of whether or not a smooth dislocation is appropriate for shallow earthquakes. This time, however, the free-surface interaction should be included in the analysis.

Many of the previous investigators of body waves from shallow events have focused their attention on the Fourier transform of the entire body-wave pulse. They employed a technique which enabled them to determine important source parameters such as seismic moment, stress drop and source dimensions from the rough characteristics of the amplitude spectrum (Hanks and Wyss, 1972; Wyss and Hanks, 1972, a and b; Molnar and Wyss, 1972; Molnar, Tucker and Brune, 1973). Since reflected or converted phases such as *pP*, *sP* or *sS* can affect both the long-period level and the shape of the amplitude spectrum, it will be important to see if the results change when the free surface is correctly accounted for.

Langston and Helmberger (1975) have outlined a simple procedure for including the surface interaction in the computation of a synthetic seismogram from a model of a shallow dislocation source. In other words, they have presented a tractable solution to the forward problem of computing the data given the model. We have demonstrated in a related work (Mellman and Burdick, 1976), that the existence of a solution to the forward

problem along with a quantitative method for comparing the synthetic to the actual data make it possible to solve the inverse problem; that is, an optimal fault model can be determined from the data by an iterative generalized linear inverse technique. We present here the result of the application of the inversion technique to the Borrego Mountain earthquake of April 9, 1968. We present a final model which accurately predicts all of the observed wave forms. We then use the model to identify a single, strong arrival in the

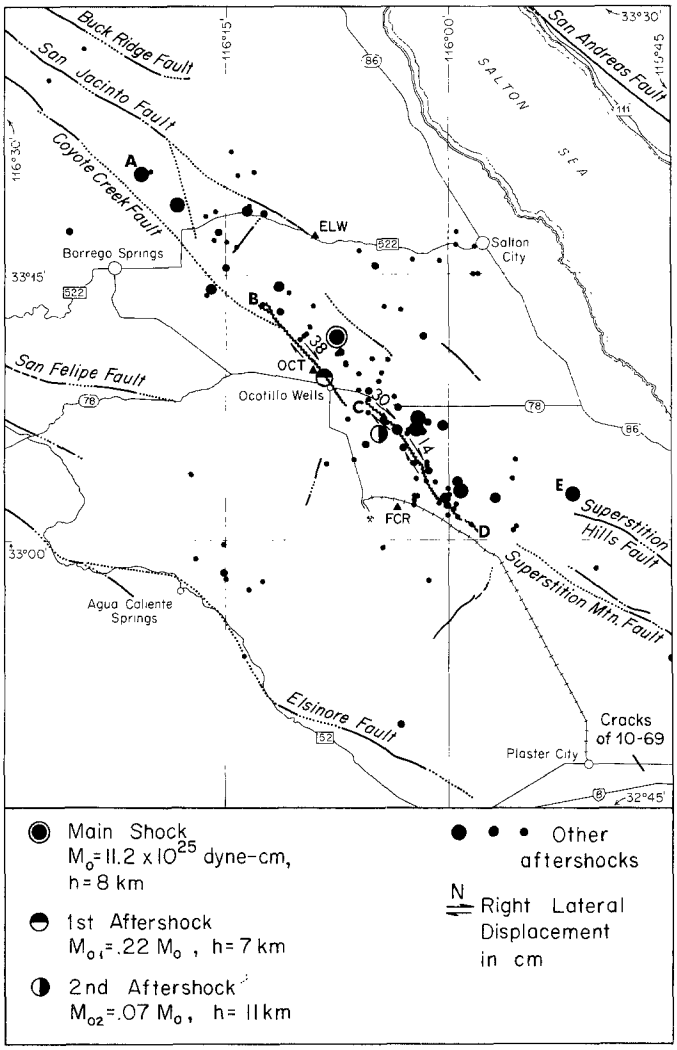

FIG. 1. The Borrego Mountain tectonic zone: Segment AE ~ 55 km marks the extent of the aftershock zone and BD ~ 31 km the total rupture length. Segment BC radiated most of the energy in the main shock. The length of this segment plus the 8-km depth of the main shock motivated the choice of a circular fault model with radius 8 km. Segment CD ~ 17 km was probably due to a swarm type event. (Figures 1 and 2 are modified from Allen and Nordquist, 1972).

record, and finally we interpret the shape of this basic seismic pulse in terms of a smooth dislocation model.

THE BORREGO MOUNTAIN EARTHQUAKE

The Borrego Mountain event was a magnitude 6.4 strike-slip earthquake which occurred at 02:29 GMT April 9, 1968 on the Coyote Creek fault in southern California. Figure 1 shows the location of the main shock as well as many of the aftershocks and the

trace of the ground breakage. After the event, both the California Institute of Technology and the USGS undertook a thorough study of all major types of postseismic phenomena. From their observations, we can draw two important conclusions which bear heavily on our interpretation of what happened during the earthquake. The first is that even though the ground breakage appears simple, the pattern of stress release was probably very complex. This can be inferred from the following points: (1) In the Imperial Valley, the San Andreas fault splays out into a number of closely interrelated faults. Each nearby zone of weakness contributes to the complexity of the stress pattern near the Coyote Creek fault (Sharp, 1972). (2) Surface offsets were observed on the Imperial, Superstition Hills and San Andreas faults as well as the Coyote Creek fault (Allen *et al.*, 1972). (3) The aftershocks had a very diffuse spatial pattern. It defined only a broad three-dimensional region of stress release instead of a single plane of failure (Allen and Nordquist, 1972; Hamilton, 1972). This complex prestress pattern seems to manifest itself in some unusual aftershocks occurring immediately after the main shock.

The second conclusion which can be made from the postseismic observations is that there was a clear difference in the behavior of the north break (segment BC in Figure 1) and the south break (segment CD in Figure 1). The north break had a large initial surface offset, relatively few aftershocks and very little postseismic creep. The south segment had a small initial offset, more aftershocks, and as much postseismic as coseismic displacement (Allen and Nordquist, 1972; Clark, 1972; Burford, 1972). Evidence in the body waves shows that these variations reflect different behaviors deep in the Earth.

The Data Set

The data set used in the inversion procedure was selected from the *P* and *SH* body-wave forms recorded at stations in the World Wide Seismograph Station Network. Recordings made outside the epicentral range of 30° to 90° were excluded to circumvent problems with upper mantle or core structure, and recordings with a signal-to-noise ratio of less than 5:1 were excluded to reduce difficulty with background noise. Processing noise was kept to a minimum by digitizing each record ten times and averaging the results. The names and locations of the stations which had records of acceptable quality are listed in Table 1 and their azimuthal spread shown in Figure 2. The stations are plotted along with the first motion data and the fault planes determined by Allen and Nordquist (1972). It is regrettable that no high-quality wave-form data was available to the southwest of the event but there was sufficient coverage to impose some heavy constraints on the allowable source mechanism. The observed wave forms are the *top traces* shown in Figure 5.

Model Parameterization and Inversion

The first step in applying linear inversion theory to a problem is to formulate a technique for computing theoretical values for the observed data from a finite number of model parameters. In the Langston and Helmberger (1975) procedure for computing synthetic seismograms for a point dislocation source, the basic parameters are a time function, source depth, and the three fault orientation parameters. If the source is to be considered as a sum of point sources, the same parameters as well as a relative size, time and location must be specified for each additional source. The origin time and epicentral location of the primary source are assumed to be known quantities, and its absolute size need not be specified if only relative wave shapes are considered. In order to obtain an adequate fit to the Borrego Mountain data, it was necessary to use a sum of three sources. This made a total of 20 parameters and three time functions which had to be specified to compute the synthetics.

The problem of parameterizing a time function can be approached in two ways. The first is to directly parameterize some pulse-like function and assume that it is independent of azimuth. The second is to use a finite source model. The free parameters in a finite source are usually the rupture velocity and average dislocation time on a failure surface with some assumed geometry. The time pulse for such a model is a function of both azimuth and takeoff angle (Fukao, 1971; Savage, 1966). The approach used in this study was to begin with a simple, azimuthally independent pulse. After an optimal model was obtained, the synthetics were compared with the data to test for any evidence which might

TABLE 1

STATION LOCATION AND AMPLITUDE DATA

Station	Azimuth from North (deg)	Wave Type	Moment ($\times 10^{-25}$ dyne-cm)	ϕ (deg)	Relative Deviation of M_o from Average*
MAT	309	*P*	17.2	6	0.53
SEO	315	*P*	16.0	0	0.42
COL	338	*P*	12.3	23	0.09
KEV	13	*P*	12.1	58	0.08
KEV	13	*SH*	9.5	58	−0.15
NUR	18	*P*	13.6	63	0.21
UME	18	*SH*	11.2	63	0.00
AKU	27	*SH*	10.5	72	−0.06
ESK	33	*SH*	10.4	78	−0.07
LOR	36	*SH*	10.2	81	−0.09
MAL	48	*SH*	10.3	87	−0.09
WES	62	*P*	12.3	73	0.09
WES	62	*SH*	9.8	73	−0.13
OGD	64	*P*	9.9	71	−0.12
OGD	64	*SH*	9.3	71	−0.17
SCP	65	*P*	11.1	70	−0.01
SCP	65	*SH*	8.3	70	−0.26
NAT	100	*P*	11.8	35	0.05
BOG	117	*P*	18.4	18	0.64
BHP	117	*P*	10.0	18	−0.11
LPB	129	*P*	11.6	6	0.03
LPB	129	*SH*	9.0	6	−0.20
ARE	132	*P*	15.0	3	0.34
ARE	132	*SH*	7.1	3	−0.37
NNA	133	*P*	12.9	2	0.15
NNA	133	*SH*	6.4	2	−0.43
LPA	136	*SH*	9.5	1	−0.16
PEL	142	*SH*	8.8	7	−0.22

*Average = 11.2; σ = 2.8.

justify an azimuthally dependent model. The azimuthally independent pulse shape chosen was a triangular pulse requiring only two parameters; a zero-to-peak time and a peak-to-zero time.

It was also necessary at the outset of the inversion procedure to choose a near-source and near-receiver earth structure. Again the decision was made to start with the simplest possible assumptions, but to continuously test for any features in the data which would justify a more complex model. More specifically, at the beginning only the rays *P*, *pP* and *sP* (or *S* and *sS*) were computed. At several points, however, the strongest rays generated

by the near-source structure proposed by Hamilton (1972) and the near-receiver structure discussed by Burdick and Helmberger (1974) were also included. No effects which could be unambiguously attributed to layered structure near the source or receiver were ever identified, so throughout this study only the five basic rays were used to compute the synthetics.

Once the model had been parameterized, it was necessary to define some quantitative measure of the correctness of a given model. This was done by first defining the correlation between a computed seismogram $S_i(t)$ and an actual seismogram $d_i(t)$ as

$$N_i = \text{Max}\left[\int_0^T S_i(t) d_i(t+\tau)\, dt\right]$$

where

$$\int_0^T S_i(t)^2 dt = \int_0^T d_i(t)^2 dt = 1$$

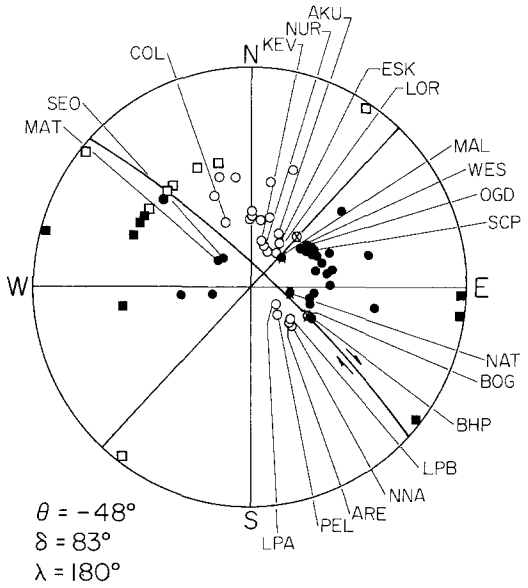

FIG. 2. The stations used in this study as they distribute with respect to the fault-plane solution determined by Allen and Nordquist (1972). Unlabeled points are other stations which they used in their first-motion study. θ is the fault strike, δ the dip and λ the rake.

T is the window length which in this case was 25 sec, and i is an index which ranged over the data set. The repeated index does not indicate a summation, The total measure of model correctness M was given by

$$M = \sum_i (1 - N_i)^2.$$

Since N_i uniquely approaches 1 when S_i approaches d_i, M goes to zero when the synthetics match the data exactly. The derivatives of M with respect to the model parameters were taken numerically and linear inversion technique applied to find an optimal model (Mellman and Burdick, 1976).

The initial attempts at inversion were made using a single point source model. The *top two traces* of Figure 3 illustrate the result for a typical seismogram. It was clear that, although the model was adequate for the first few seconds, there was much more structure present in the later portion of the seismogram than was predicted by the synthetic. This

could have been the result of either a complicated earth structure or a more complicated source mechanism. On the *right* in the third row of Figure 3 is shown the synthetic including the effects of assuming that the Hamilton (1972) crust model exists near the source, and on the *left* is the result of including a second point source. In the lowest row, the result of including three point sources is shown as opposed to including both the near-source and near-receiver crustal effects (see Table 2). The effects of introducing appropriate earth structure were always too small to explain the discrepancies between the synthetics for a one source model and the observations. We concluded that the structure late in the wave forms was probably caused by the first large aftershocks. We attempted to model the first two with additional point sources.

The previously published mechanism for the Borrego main shock was used as a starting model for the single point-source inversion runs. When it became apparent that a multiple point-source model would be necessary, the seismograms were examined to determine the

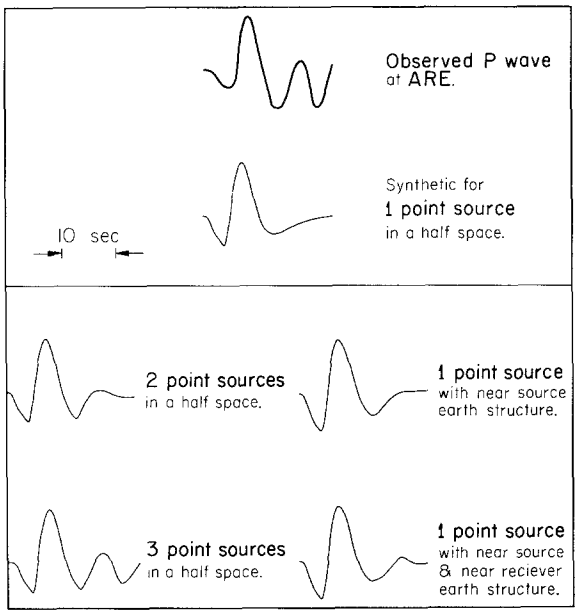

FIG. 3. The *top* of the figure shows that a single point source cannot account for the structure late in the seismogram. The *left column* shows that it is possible to obtain a better fit by adding additional point sources while the *right* shows that inclusion of the rays generated by the near-source crustal structure (Hamilton, 1972) and an appropriate near-receiver structure does not.

time when the data first began to diverge from its predicted behavior. A new point source was postulated to have occurred at that time. It was initially presumed to have had the same location as the main shock. The space of possible fault plane solutions for the second source was then explored by trial and error using a crude spacing between models. Synthetics were computed for only a few key observations. When a roughly satisfactory model had been determined, the inversion procedure was used to iterate in on a more refined model for the location, time, time function and fault-plane solution of the shock. The same procedure was used on the second aftershock. We stress that there can be no way of insuring that the models found by this method are in any way unique. However, as we shall show, they do predict the fine details of the observed wave forms very closely. Also, we can state that in our rough search of the model space we did not find any other model which came nearly as close to predicting the data as the one presented in the following section.

The Final Model

In the second row of Figure 5 are the synthetic wave forms for the final model. Those arrivals which are marked are the direct arrivals and the primary reflections from the main shock. The later complications in the wave form are caused by the later shocks. The wide variety in the appearance of the secondary structure provides an additional indication

TABLE 2

Velocity Models

Layer	V_p (km/sec)	V_s (km/sec)	ρ (g/cc)	Th (km)	(T/Q_s) average	(T/Q_p) average
			Half-Space Model			
1	6.1	3.5	2.7	∞	1.3	5.2
			Hamilton Crustal Model			
1	2.5	1.6	1.4	0.4	—	—
2	5.1	3.0	2.3	2.5		
3	6.0	3.5	2.7	11.1		
4	7.1	4.2	3.2	11.0		
5	7.9	4.6	3.6	∞		
			Near Receiver Crustal Model			
1	6.28	3.63	2.87	37	—	—
2	7.96	4.60	3.37	∞		

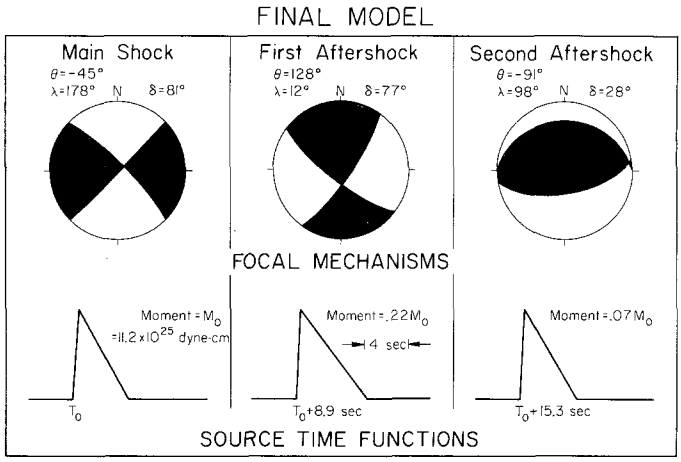

FIG. 4. The fault-plane solutions and the time functions of the main shock and the first two aftershocks. The shaded portions of the circles represent the compressional quadrants. The fault orientation parameters have been defined in Langston and Helmberger (1975).

that it is a manifestation of source and not crustal complexity. A strong arrival from a sharp layer always arrives at nearly the same point on the record and generally varies slowly as a function of azimuth: but a secondary source predicts three arrivals, *P*, *pP*, and *sP* whose interaction can vary rapidly with azimuth. The final source locations, time functions and fault planes used in computing the synthetics are shown in Figures 1 and 4.

Given that structure-generated arrivals on the order of those shown in Figure 3 have been neglected, the fit to the data appears most satisfactory. For each peak in the data,

there is a corresponding peak of the right duration and sign in the synthetics. The worst fits both in terms of visual appearance and the correlation N_i occur for the P wave forms at stations where P and pP arrive with the same polarity. These include MAT, SEO, LPB, ARE and NNA. Their common feature is that they lie off the very ends of the fault trace. They are composed of rays which travel directly along the fault plane (see Figure 2). As Figure 5 shows, the difficulty is that the predicted ratio of the peaks $sP/(P+pP)$ is too small with respect to the observed values. There is no way to determine whether this occurs because of anomalously large S or anomalously small $(P+pP)$ without the use of absolute amplitude measurements.

A value for M_o, the seismic moment of the first source, can be determined from a measurement of the absolute amplitude at each station by use of the formula

$$M_o = \frac{A_{\text{observed}}}{A_1}$$

A_{observed} is the observed amplitude of either the sP or the $S+sS$ peak and A_1 is the theoretical amplitude of the same peak for an event with moment one. The moment values determined from the 28 observations used in the inversion are listed in Table 1. They have an average value of 11.2×10^{25} dyne-cm and a standard deviation of 2.8×10^{25} dyne-cm.

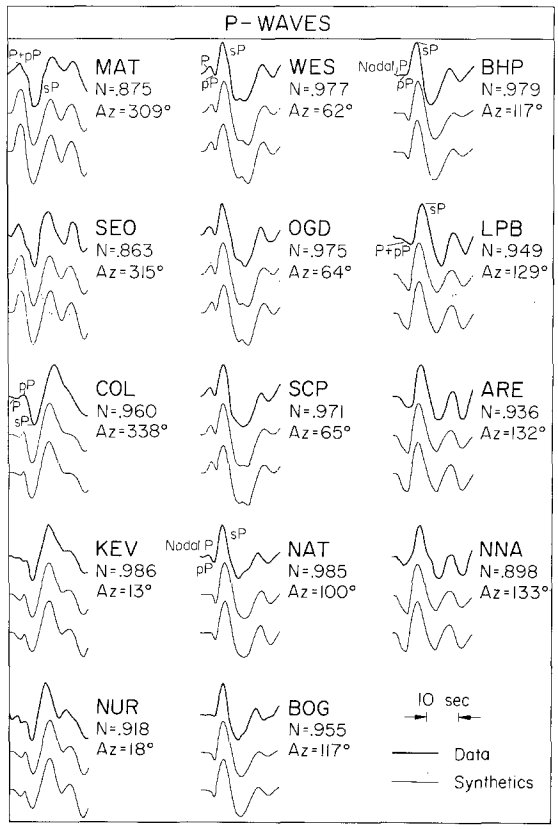

FIG. 5a. The observed P waves (*top*) predicted by the final (3 point sources with azimthally independent time functions) model (*middle*) and the synthetics predicted by the same model with the main shock represented by a finite (azimuthally dependent time function) source model (*bottom*). The quantity N_i is the normalized correlation operator which uniquely approaches 1 as the synthetic approaches the data. The azimuths are measured from north.

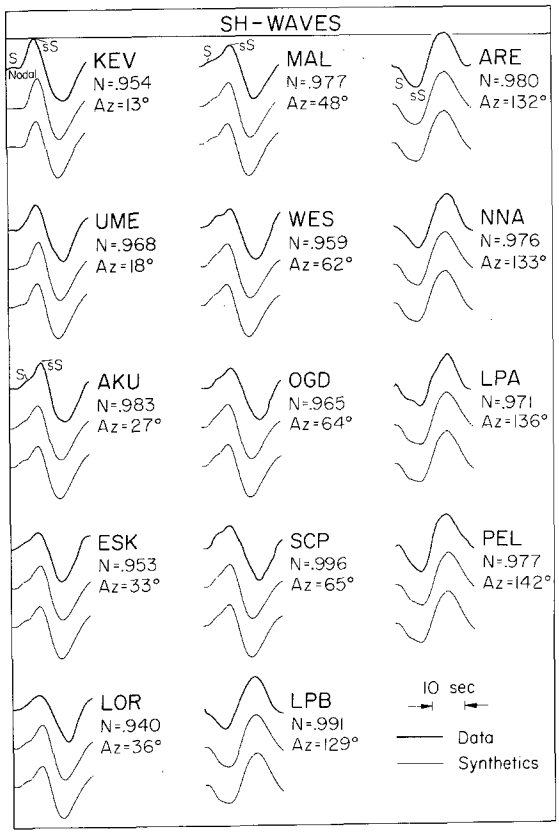

FIG. 5b. The observed *SH* waves (*top*) predicted by the final model (*middle*) and the synthetics predicted by the same model with the main shock replaced by a finite source model. The labeled arrivals in both Figure 5a and Figure 5b are from the main shock. In both figures, the stations are shown in order of increasing azimuthal deviation from the NW extension of the fault trace (see Figure 2).

The relative errors between the amplitude computed assuming the average moment and the observed amplitude are plotted against an azimuthal angle ϕ in Figure 6. This angle is defined to be zero for stations directly off either end of the fault and to have a maximal value of 90° for stations in a direction perpendicular to the fault. The observed values of sP tend to be too large and the observed values of $S + sS$ too low whenever those rays travel directly along the fault zone. It is important to note that most of the tectonic features in the region also trend parallel to the fault. The implication is that the ratio of the amplitudes of SV to SH is sensitive to the lateral variations induced by the fault itself or by some other tectonic feature. Since the sP phase is often the dominant one in the far-field P wave form, this instability may be responsible for anomalies in P-wave shape and amplitude as well as in the S.

The fault plane determined for the main shock (Figure 4) is virtually identical to the one determined from the first-motion data by Allen and Nordquist (1974). The strike of the northwest-trending plane corresponds closely with the strike of ground breakage, and the motion indicated by the conjugate plane corresponds with most of the observed offsets. There can be little doubt that the northwest plane is highly representative of the actual plane of failure. Because of the information in the body waves about the separation of P, sP and pP, the depth can be constrained to be between 7 and 9 km.

The second shock was apparently a left-lateral, strike-slip event occurring 9 sec after the

first. The location is very poorly constrained, since it did not occur far enough away from the main shock to cause obvious azimuthal dependence in its arrival time (Figure 1). As shown in Figure 4, it seems to have released a stress nearly reversed to that of the main shock. There are several indications from other types of data that such an event might have occurred. First, there were observations of ground displacement near point B with a left lateral component which was clearly not of the Reidel type (Clark, 1972). Second, there are the previously cited lines of evidence which suggest complex prestress and stress release patterns in which reversed stresses might easily have developed. Sharp (1972) mentions several instances where left-lateral strain buildup had been reported in the region in the past. Finally, studies by Burridge (1969) and Madariaga (1976) have shown that it is theoretically possible for reversed or overshoot-type stresses to develop even in relatively simple cases.

The third shock which occurred approximately 15 sec after the first was a thrust event

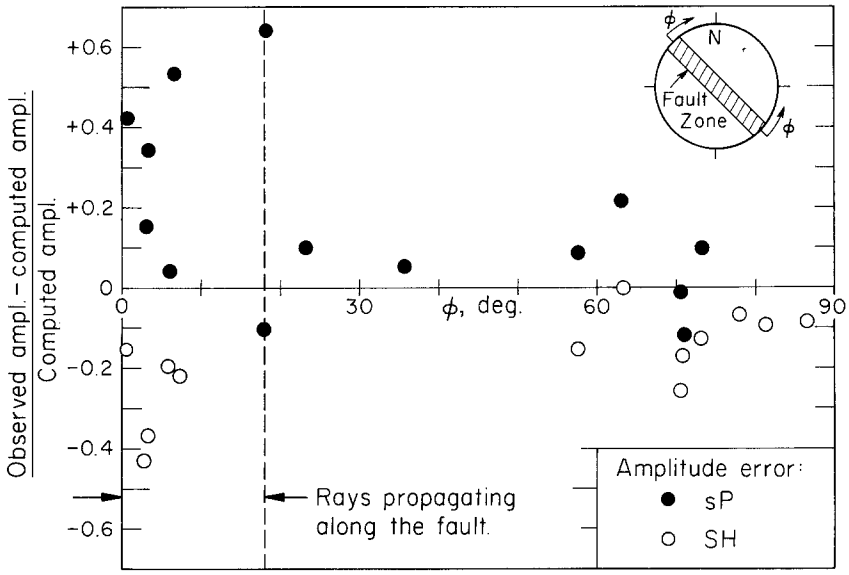

FIG. 6. The dependence of the scatter in the amplitude data on the azimuthal angle ϕ which is defined so that it becomes small whenever rays propagate along the fault zone. The final model can predict observed amplitudes to within 25 per cent except at stations with low values of ϕ.

(Figure 4). This mechanism is consistent with the stress pattern which induced the first event in that the major axis of compression is roughly similar. The location is again very poorly constrained by the far-field data, but it appears that the shock occurred near point C in Figure 1. The surface break takes a sudden step to the left and shows an abrupt decrease in total offset at this point. Also, one of the later aftershocks which occurred there was a thrust event with a mechanism similar to this one (Hamilton, 1972). These are the first of several correlations that were found between details of the postseismic observations and the final source model. The second shock had a moment only a quarter as large as the first, and the third less than a tenth of the first. Since they were much smaller, they had a relatively minor effect on the wave form and on the surface break. In effect, they are nothing more than the first and second aftershocks. The first event which radiated the most energy determined the first motions and the gross features of both the wave forms and the ground breakage.

A Finite Source Model

We return now to the initial question of what type of finite source model is appropriate for shallow earthquakes. We will attempt to model the first source since it was the largest. Figure 5 shows that it would be difficult to separate the direct P pulse from the pP or the S from the sS. The sP, however, is strong enough to be relatively clear on the record. We present here an attempt to determine a model which fits the characteristics of that one phase. Then we use the model to compute the complete seismograms for comparisons with the data and the inversion result.

Several different techniques were used to attempt to find azimuthal dependence in the duration of the sP pulse as was done for P waves from deep earthquakes by Mikumo (1971 a, b). No clear azimuthal pattern was resolved by any of these means. The effect is apparently too small to be seen over the noise level. Any inferences to be made about the finiteness of the source will have to come from the shape or frequency content of the time function. This type of analysis requires a better estimate of the shape of the source-time function than the crude result from the inversion. A much better determination was

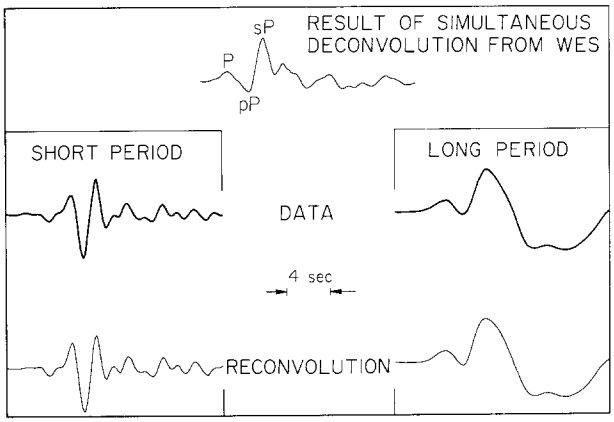

Fig. 7. (*Top*) A time function which is compatible with both the long-period and short-period records from WES. It was obtained by Fourier transforming both records (*middle traces*), dividing out the instrument and Q filter from each, taking a weighted average of the results and inverse transforming. When the *top* trace is reconvolved with the appropriate instrument and Q it produces the *bottom* traces.

obtained by making use of the high quality recording from WES. At this station, both the long- and short-period recordings were strong, clear and virtually free of noise. As illustrated in Figure 7, a time function was obtained by a simultaneous deconvolution technique which could be reconvolved with either the short- or long-period instrument to reproduce the data. The deconvolution technique consists of transforming equivalent segments of the long-period and short-period records into the frequency domain, dividing each by the appropriate instrument and Q responses, weighting, averaging, and inverse transforming. The weighting function for the long-period instrument was equal to one for frequencies less than 0.25 Hz, and it fell off linearly from that frequency to zero at 0.5 Hz. The short-period weighting function was just one minus the long-period function. A correction was made for any difference in reference time between the two record segments by solving for the pure phase delay which made the long-period record's phase curve most like that of the short-period in the crossband of 0.25 to 0.50 Hz. The portion of the deconvolved time function which is dominated by the first source sP is compared with the inversion result in Figure 8.

The deconvolution result bears a strong resemblance to the time function for a circular fault published by Savage (1966). The third trace in Figure 8 is the theoretical time function for a circular rupture propagating on the fault plane at 2.8 km/sec (0.8 β) to a final radius of 8 km. The dislocation-time history is assumed to be a step and the final offset is assumed to die off as $(1-(r/R)^2)^{1/2}$. Figure 1 shows that this would correspond to a rupture beginning at the hypocenter, propagating up to the surface, and downward by an equal amount, northwest to point B and southeast only to point C. The time function for an ellipsoidal fault surface extending all the way down to point D is too long in duration to be compatible with the inversion or deconvolution result as shown at the bottom of Figure

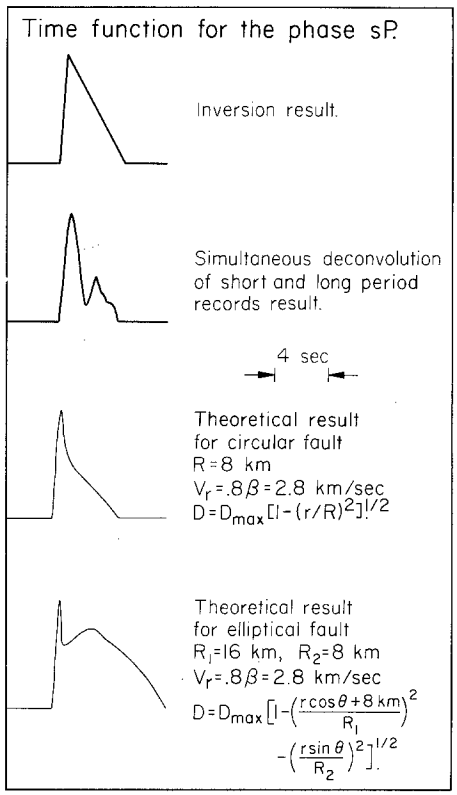

FIG. 8. *sP* time functions for the station WES obtained from inversion and simultaneous short period-long period deconvolution as opposed to theoretical results for a circular fault large enough to extend over segment BC in Figure 1 and on eliptical fault large enough to cover BD. D_{max} is the maximum displacement, and r and θ are cylindrical coordinates on the fault surface. The average time history for the theoretical models is a step function.

8. The implication is that segment CD did not contribute significantly to the energy in the body-wave pulse. If the rupture velocity had been assumed to be β instead of 0.8 β, the fault radius would only have had to be increased to 9 km to keep the pulse duration the same. Therefore, this result is not dependent on the assumed rupture velocity. There is abundant evidence in the postseismic observations that the two segments behaved in different fashions. The more southern segment showed a much smaller initial offset, extensive postseismic creep, and a higher level of aftershocks. We infer that the southern segment initially absorbed most of the stress load induced by the brittle failure of the north segment but then released it slowly. Some failure must have occurred sometime in the first few hours

to account for the initial surface offset observations, but the creep movement extended over a period of months. It seems as though the southern portion of the Borrego event was very similar to the nearby Brawley swarm event studied by Johnson and Hadley (1976).

It should be noted that we are not including in our calculations the correction for the fact that the two sides of the fault have a finite slip velocity. One approximate way to do this would be to convolve a boxcar of roughly the same duration as the average slip time with the theoretical pulses. The total rupture time would have to be decreased by a corresponding amount to keep the total duration of the pulse consistent with the observations. This would mean that the estimated radius would be even smaller. In this sense, the value of 8 km should be considered as an upper bound.

The complete synthetic seismograms predicted by the finite source model are the *bottom traces* in Figure 5. They appear to fit just as well as the ones computed from the point source model. The predicted azimuthal dependence of pulse duration is very slight which explains why this effect was so difficult to observe in the data.

Assuming that the first shock had a moment of 11.2×10^{25} dyne-cm and a radius of about 8 km, and if μ was approximately 3.4×10^{11} gm/cm sec^2 then the average displacement must have been

$$D_{av} = \frac{M_o}{\mu \pi R^2} = 164 \text{ cm}.$$

This value is four times as large as the observed surface offsets implying that the displacements decreased as the rupture propagated upward. Since for the theoretical model considered here, displacement varies along the fault as $D = D_{\text{Max}} (1 - (r/R)^2)^{1/2}$, the largest displacement was

$$D_{\text{Max}} \sim \tfrac{3}{2} D_{\text{av}} = 246 \text{ cm}.$$

Keilis-Borok (1959) has formulated an expression for the stress-drop from a dislocation of this type.

$$\Delta\sigma = \frac{7\pi}{24} \frac{D_{\text{Max}}}{R} \mu$$

assuming that $\lambda = \mu$. This gives a stress drop of $\Delta\sigma = 96$ bars. Kanamori and Anderson (1975) have compiled a list of stress-drop determinations for a large number of earthquakes. The values scatter between 10 and 100 bars, so the Borrego Mountain earthquake falls within the range of previous determinations. However, they have noted that most interplate earthquakes fall toward the low end of the range. In this sense, the event is somewhat anomalous. It remains to be seen whether other earthquakes also give higher values of $\Delta\sigma$ when analyzed using the techniques used in this study.

Conclusions

The purpose of this study was twofold. The first was to identify and characterize all of the different elements which control the shape of the body waves from a shallow earthquake. The second was to isolate an arrival which was not strongly contaminated by other arrivals and to model this single arrival with a finite dislocation source. In pursuing the first of these, we found that reflections from the free surface play a dominant role in shaping the pulse, but also that arrivals from the first large aftershocks could be observed in the wave form. This result is not too remarkable since there is no reason to expect a long delay between the termination of the main shock and the initiation of the aftershock

sequence. In pursuing the second goal, we decided to construct a model for the sP phase from the main shock. A smooth dislocation proved to be adequate to model the pulse just as in the case of most deep earthquakes.

The fault parameters of the Borrego Mountain event were previously determined using the spectral characteristics technique by Hanks and Wyss (1972), and by Wyss and Hanks (1972a). They analyzed the P and S data separately which gave two different values for each parameter. Their moment values of $M_o(P) = 10 \times 10^{25}$ dyne-cm and $M_o(S) = 6.6 \times 10^{25}$ dyne-cm compare favorably with the value from this study of 11.2×10^{25} dyne-cm. However, this agreement is probably fortuitous, since the moments they determined were based on the long-period level Ω_o of the amplitude spectrum of the entire P or S waveforms. This means that they interpreted the sum $\Omega_o(P) + \Omega_o(pP) + \Omega_o(sP)$ as though it were only $\Omega_o(P)$ and the sum $\Omega_o(S) + \Omega_o(sS) + \Omega_o(pS)$ as though it were only $\Omega_o(S)$. Their values for the fault radius, $R(P) = 14$ km and $R(s) = 23$ km, are significantly larger than the $R = 8$ km result of this study. Therefore, they computed a stress drop $\Delta\sigma$ of only 6 bars as compared to the $\Delta\sigma = 96$ bars result obtained here. It is encouraging that when the free surface is properly accounted for, it is not necessary to use different source parameters for S and P.

The relatively small value of $R = 8$ km was chosen to give an appropriate fit to the shape and duration of the observed sP pulse. As we have discussed, an 8-km fault radius does not conflict with the postseismic observations, if the CD segment of the fault is assumed to be a creep or swarm event. If this analysis is correct, it means that it is necessary to be cautious about inferring fault dimensions from rupture lengths or aftershock zones.

Finally, we have demonstrated the adequacy of a shallow double-couple point-source model in predicting wave shapes. The only breakdowns occur when observations are made near nodes. One of the mechanisms of breakdown is apparently instability in the polarization of the S motion induced by lateral structure. Since sP sometimes dominates the P wave form, this can cause anomalies in the P waves as well as the S waves.

Acknowledgment

The authors thank D. V. Helmberger, T. Heaton, and C. Langston for their advice during this study and for critically reading the manuscript. This research was supported by the Advanced Research Projects Agency of the Department of Defense and was monitored by the Air Force Office of Scientific Research under Contract F44620-72-C-0078.

References

Allen, C. R. and J. M. Nordquist (1972). Foreshock, main shock and larger aftershocks of the Borrego Mountain earthquake, *U.S. Geol. Surv. Profess. Paper 787*, 16–23.

Allen, C. R., M. Wyss, J. N. Brune, A. Grantz, R. E. Wallace (1972). Displacements on the Imperial, Superstition Hills, and San Andreas faults triggered by the Borrego Mountain earthquake, *U.S. Geol. Surv. Profess. Paper 787*, 87–104.

Burdick, L. J. and D. V. Helmberger (1974). Time functions appropriate for deep earthquakes, *Bull. Seism. Soc. Am.* **64**, 1419–1428.

Burford, R. O. (1972). Continued slip on the Coyote Creek fault after the Borrego Mountain earthquake, *U.S. Geol. Surv. Profess. Paper 787*, 105–111.

Burridge, R. (1969). The numerical solution of certain integral equations with nonintegrable kernals arising in the theory of crack propagation and elastic wave diffraction, *Phil. Trans. Roy. Soc. (London), Ser. A.* **265**, 353–381.

Clark, M. M. (1972). Surface ruptures along the Coyote Creek fault, U.S. *Geol. Surv. Profess. Paper 787*, 55-86.

Fukao, Y. (1971). Seismic body waves from surface faults, *J. Phys. Earth* **19**, 271–281.

Hamilton, R. M. (1972). Aftershocks of the Borrego Mountain earthquake from April 12 to June 12, 1968, *U.S. Geol. Surv. Profess. Paper 787*, 31–54.

Hanks, T. C. and M. Wyss (1972). The use of body-wave spectra in the determination of seismic-source parameters, *Bull. Seism. Soc. Am.* **62**, 561–589.

Helmberger, D. V. (1974). Generalized ray theory for shear dislocations, *Bull. Seism. Soc. Am.* **64,** 45–64.

Hudson, J. A. (1969). A quantitative evaluation of seismic signals at teleseismic distances, I. Radiation from point sources, *Geophys. J.* **18,** 233–249.

Johnson. C. E. and D. M. Hadley (1975). Tectonic implications of the Brawley earthquake swarm, Imperial Valley, California, January 1975, *Bull. Seism. Soc. Am.* **66,** 1133–1144.

Kanamori, H. and D. L. Anderson (1975). Theoretical basis of some empirical relations in seismology, *Bull. Seism. Soc. Am.* **65,** 1073–1095.

Keilis-Borok, V. (1959). On estimation of the displacement in an earthquake source and of source dimensions, *Ann. Geofis. (Rome)* **12,** 205–214.

Langston, C. A. and D. V. Helmberger (1975). A procedure for modelling shallow dislocation sources, *Geophys. J.* **42,** 117–130.

Madariaga, R. (1976). Dynamics of an expanding circular fault, *Bull. Seism. Soc. Am.* **66,** 639–666.

Mellman, G. and L. J. Burdick (1976). Inversion of body waves to fault models (in preparation).

Mikumo, T. (1971a). Source processes of deep and intermediate depth earthquakes as inferred from long period *P* and *S* wave forms, I, *J. Phys. Earth* **19,** 1–19.

Mikumo, T. (1971b). Source processes of deep and intermediate earthquakes as inferred from long period *P* and *S* wave forms, *J. Phys. Earth* **19,** 303–320.

Molnar, P., Tucker, B. E., and J. N. Brune (1973). Corner frequencies of *P* and *S* waves and models of earthquake sources, *Bull. Seism. Soc. Am.* **63,** 2091–2104.

Molnar, P. and M. Wyss (1972). Moments, source dimensions and stress drops of shallow focus earthquakes in the Tonga-Kermadec Arc, *Phys. Earth Planet Interiors* **6,** 263–278.

Savage, J. C. (1966). Radiation from a realistic model of faulting, *Bull. Seism. Soc. Am.* **56,** 577–592.

Sharp, R. V. (1972). Tectonic setting of the Salton Trough, *U.S. Geol. Surv. Profess. Paper 787*, 3–15.

Teng, T. L., and A. Ben-Menahem (1965). Mechanism of deep earthquakes from spectrums of isolated body wave signals, *J. Geophys. Res.* **70,** 5157–5170.

Wyss, M. and T. C. Hanks (1972a). Source parameters of the Borrego Mountain earthquake, *U.S. Geol. Surv. Profess. Paper 787*, 24–30.

Wyss, M. and T. C. Hanks (1972b). The source parameters of the San Fernando earthquake inferred from teleseismic body waves, *Bull. Seism. Soc. Am.* **62,** 591–602.

SEISMOLOGICAL LABORATORY
CALIFORNIA INSTITUTE OF TECHNOLOGY
PASADENA, CALIFORNIA 91125
DIVISION OF GEOLOGICAL AND PLANETARY
SCIENCES CONTRIBUTION NO. 2711

Manuscript received February 25, 1976